Musa acuminata peel extract mediated eco-friendly synthesis of solar light-active ZnO nanosponge for enhanced dyeing wastewater degradation

Jin-Chung Sin[1,3*], *Ka-Wey* Ong[1], *Sze-Mun* Lam[2,3], and *Honghu* Zeng[3]

[1] Department of Petrochemical Engineering, Faculty of Engineering and Green Technology, Universiti Tunku Abdul Rahman, Jalan Universiti, Bandar Barat, 31900 Kampar, Perak, Malaysia
[2] Department of Environmental Engineering, Faculty of Engineering and Green Technology, Universiti Tunku Abdul Rahman, Jalan Universiti, Bandar Barat, 31900 Kampar, Perak, Malaysia
[3] College of Environmental Science and Engineering, Guilin University of Technology, Guilin 541004, China

Abstract. ZnO nanosponge was synthesized for the first time via a green method using *Musa acuminata* peel extract. The X-ray diffraction, Raman, energy dispersive X-ray and fourier-transform infrared analyses demonstrated that the synthesized sample was well crystallized and possessed hexagonal wurtzite pure ZnO. The field-emission scanning electron microscopy observation revealed that the ZnO nanosponge was assembled by aggregated spherical particles with sizes of 30-128 nm. Under simulated solar light irradiation, the ZnO nanosponge acted as an excellent photocatalyst for methylene blue and rhodamine B mixtures degradation compared to commercially available TiO_2-P25. The enhanced photocatalytic activities of ZnO sample can be attributed to the high generation of hydroxyl radicals as a result of its unique sponge-like porous structure with large surface area. Furthermore, the ZnO nanosponge can be used effectively on the photodegradation of real textile dye wastewater. These characteristics showed that the biosynthesized ZnO nanosponge can be employed as a photocatalyst for environmental remediation.

1 Introduction

A large volume of non-biodegradable organic dyes was utilized in the textile, leather, food, paper, pharmaceutical and plastic industries. The dye effluents from these industries were strongly coloured, which can hinder the photosynthesis of aquatic plants and caused deterioration of water quality. Furthermore, the carcinogenic and toxic effects of these dyes rendered them cancer-causing properties [1]. Hence, discharge of these hazardous coloured effluents without proper treatment has resulted to a surge in water contamination, which has become a global environmental issue. Among various treatment methods, heterogeneous photocatalysis has been proven as an effective technology in degrading harmful heavy organic contaminants due to its high oxidation efficiency and low energy consumption [2, 3]. The photocatalytic technology was also harmless to the environment as the contaminants can be decomposed into non-toxic molecules such as CO_2 and H_2O. As a significant functional oxide, ZnO has garnered great attention as a photocatalyst owing to its large band gap (~3.3 eV), good catalytic properties and low cost [4]. Particularly, nanoscale ZnO which has a large specific surface area, offering more reaction interface compared to bulk materials [4]. Over the past few years, nanoscale ZnO with different structures and morphologies have been widely produced by chemical approaches such as co-precipitation, sol-gel and sonochemical processes [5, 6]. Nevertheless, these approaches involved the use of toxic solvents that were hazardous to the environment. Recently, biosynthesis has garnered enormous scientific attention as an eco-friendly, inexpensive and less toxic route of fabricating nanoscale ZnO from biodegradable materials [7-9]. For example, Anbuvannan et al. [7] reported on the *Anisochilus carnosus* leaf extract-mediated synthesis of ZnO nanoparticles where they revealed that their synthesized materials had excellent photocatalytic and antibacterial properties. It has also been reported that the zinc precursor was employed as an oxidant and the phytochemicals in the plant extract served as reducing agents during the ZnO synthesis. Patil et al. [8] fabricated flower-like ZnO nanostructures possessing virtuous photocatalytic activity for the methylene blue degradation by an *Azadirachta indica* extract-mediated hydrothermal method. To our knowledge, nevertheless, the biosynthesis of nanoscale ZnO using *Musa acuminata* peel extract for photocatalytic applications has rarely been reported.

In this work, ZnO nanosponge was prepared via a green biosynthesis route using *Musa acuminata* peel extract for the first time. *Musa acuminata* came from Musaceae family and it grew very well in Asian countries mostly in India, China, Philippines and Malaysia. Additionally, the extracts of *Musa acuminata* peel contained essential phytochemicals such as flavonoids,

* Corresponding author: sinjc@utar.edu.my

phenols and L-ascorbic acid which can act as reducing agents in the catalyst synthesis [10, 11]. The physicochemical and optical properties of the sample were analyzed using different characterization measurements. The photoactivities of the ZnO sample were assessed toward binary mixture of methylene blue and rhodamine B (MB-RhB) degradation under simulated solar light irradiation. Finally, to evaluate the performance in wastewater treatment, the as-synthesized ZnO was applied for the photodegradation of real textile dye wastewater.

2 Experimental

2.1 Extract preparation and biosynthesis of ZnO nanosponge

Firstly, *Musa acuminata* peels were obtained from local market, Kampar, Malaysia. They were washed thoroughly with deionized water to remove dust and impurity from the surface. The peels were then chopped into small pieces and dried at room temperature. 50 g of finely chopped peels were added into 100 mL deionized water and boiled at 80ºC for 30 min for the preparation of *Musa acuminata* peel extract. The resulting extracts were then cooled to room temperature, filtered and used for the biosynthesis of ZnO nanosponge.

In the next step, 70 mM of $Zn(NO_3)_2$•$6H_2O$ was added into 100 mL *Musa acuminata* peel extract under vigorous stirring. The reaction was further conducted for 24 h by keeping at 80ºC. The resulted brown gel was air dried and calcined at 450ºC for 2 h in a muffle furnace and finally grounded with a pestle in a mortar to obtain the white ZnO powder.

2.2 Characterization

The sample was analyzed by X-ray diffraction (XRD, Philips PW1820), Raman scattering (Renishaw inVia Raman), field-emission scanning electron microscopy (FESEM, JEOL JSM-6701F), energy-dispersive X-ray (EDX, Oxford X-MAX), UV-vis diffuse reflectance spectroscopy (UV-vis DRS, Perkin–Elmer Lambda 35 UV–visible spectrometer), fourier-transform infrared (FTIR, Thermo Scientific Nicolet IS10) and nitrogen adsorption-desorption (Micrometrics ASAP 2020).

2.3 Photocatalytic experiments

The photocatalytic performance of the sample was examined by analyzing the MB-RhB mixtures degradation under simulated solar irradiation. A 80 W outdoor lamp with light intensity of 11,000 lx, as determined using digital luxmeter was used as irradiation source. In a typical photocatalytic experiment, 200 mg ZnO or commercial TiO_2-P25 was added into a beaker containing 200 mL of the dye mixtures solution. Before the irradiation, the suspension was dispersed in the dark for 30 min in order to attain adsorption equilibrium. During light irradiation, 4 mL of solution was sampled at given time intervals and then centrifuged to separate the suspended solids. The RhB and MB concentrations were measured using a UV-vis spectrophotometer at wavelength of 554 nm and 666 nm, respectively. The chemical oxygen demand (COD) during the dye mixtures degradation was also monitored to determine mineralization efficiency.

The photodegradation of textile dye wastewater was performed using the same procedure as above. The dye wastewater was obtained from a fabric textile plant situated in Pulau Pinang, Malaysia. The COD analysis was carried out by high-range COD vial. 2 mL of textile dye samples were placed into the COD vial and then digested at 150ºC for 2 h. For BOD_5 investigation, the samples were incubated for 5 days at 20ºC. The BOD_5 was manometrically determined using BOD Trak II™ instrument. Moreover, the NH_3-N analysis was conducted together with Nessler reagent via a UV-vis spectrophotometer at 425 nm. Finally, the colour of the degraded textile dye wastewater was measured based on colorimetric platinum cobalt method.

2.4 Determination of hydroxyl radicals (•OH)

Alkaline solution of terephthalic acid (TA) was prepared in a dilute NaOH solution (2×10^{-3} M) to ensure complete dissolution. The concentration of TA was set at 5×10^{-4} M. 200 mg catalyst was stirred in 200 mL of TA solution and irradiated for 180 min. A Perkin-Elmer Lambda S55 spectrofluorometer was utilized to monitor the photoluminescence (PL) emission using an excitation wavelength of 315 nm. The 2-hydroxyterephthalic acid displayed at 425 nm and the PL intensity was relative to the amount of •OH radicals produced.

3 Results and discussion

3.1 Characterization of ZnO sample

The phase structure and crystalline nature of the sample were analysed using XRD as shown in Fig. 1a. The crystalline peaks recorded at 2θ values of 31.8º, 34.4º, 36.3º, 47.5º, 56.5º, 62.8º, 66.3º, 67.9º and 69.0º were well corresponded to the (100), (002), (101), (102), (110), (103), (200), (112) and (201) planes, respectively. These XRD peaks indicated that the sample had typical hexagonal wurtzite structure and confirmed the formation of ZnO (JCPDS Card no. 36-1451). The intense peaks also indicated that the sample was well crystallized. No impurity phases were identified in the pattern, demonstrating the single phase and high purity of the sample. To further confirm the formation of ZnO, Raman analysis has also been conducted on the sample (Fig. 1b). A main strong peak at 437 cm^{-1} was known as nonpolar optical phonon of E_2H mode, indicating the characteristic peak of wurtzite ZnO [12]. The peaks appeared at 331 cm^{-1} and 383 cm^{-1} in the Raman spectrum were corresponded to the E_2H–E_2L and A1 (TO) phonon, respectively [13]. A weak peak observed at 583 cm^{-1} was the contribution from the E_1L mode which related to the oxygen deficiency [14].

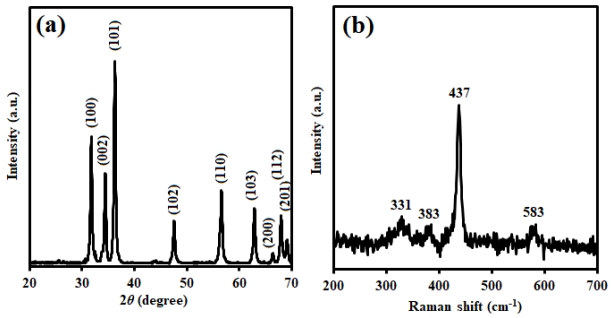

Fig. 1. (a) XRD pattern and (b) Raman spectrum of ZnO nanosponge

The morphology of the sample was analyzed by FESEM as shown in Figs. 2a-c. It was clear that the sample has a porous nature with sponge-like structure. The spongy nature of the as-synthesized sample perforated by 26–602 nm pores, which could be due to the release of volatile gases during the heat treatment [15]. The magnified image indicated that the sponge-like structure assembled by aggregated particles which were more or less spherical in shape having the sizes in the range of 30-128 nm. The chemical composition of the sample has been provided by EDX spectrum. As shown in Fig. 2d, well-defined peaks of Zn and O confirmed the formation of ZnO. Moreover, a signal of C was also identified, which can be accredited to the presence of biomolecules such as flavonoids, phenols and L-ascorbic acid in the extract. The C signal could also be associated to the carbon tape employed in the EDX characterization.

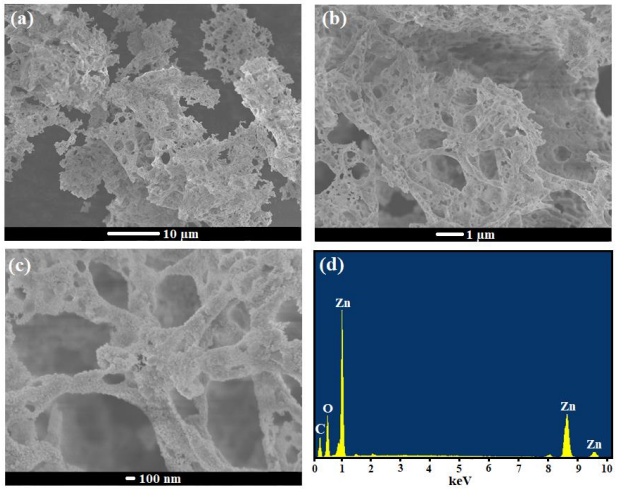

Fig. 2. (a-c) FESEM images and (b) EDX spectrum of ZnO nanosponge

Fig. 3a depicts the FTIR spectrum of the samples in the range of 4000-400 cm^{-1}. The formation of ZnO was further verified at peak 474 cm^{-1}, which represented the stretching of Zn-O band. Two absorption peaks observed at 1636 and 3442 cm^{-1} can be attributed to the -OH groups and H_2O molecules intensely bounded to photocatalyst surface. The adsorption of water molecules by the synthesized sample could indicate the ZnO nanosponge possessed large surface area. Further, weak peaks located at 1395 and 2931 cm^{-1} indicated the existence of C-O-H and C-H bonds in peel extract, respectively [16, 17].

The optical property of the samples was evaluated via UV-vis DRS spectrum as shown in Fig. 3b. The spectrum indicated that the absorption edge was positioned at 372 nm. The optical band gap of the samples was measured using Kubelka-Munk function $F(R) = (1\text{-}R)^2/2R$, where $F(R)$ is relative to the extinction coefficient (α) and R is the reflectance. A graph plotted between $(F(R)hv)^{1/2}$ versus hv and the optical band gap was obtained by extrapolating the linear portion of the curve to the photon energy axis. The band gap energy was 3.31 eV (Fig. 3b inset), which was consistent with the reported value in literatures [3, 18].

Fig. 3c exhibits the N_2 adsorption–desorption isotherms of samples. The surface area of ZnO nanosponge was determined by Brunauer–Emmett–Teller (BET) technique while the pore size distribution and pore volume were determined by Barrett–Joyner–Halanda analysis. Accordingly, the surface area of the sample was 26.3 m^2/g whereas the pore diameter and pore volume were measured to be 27 nm and 0.05 cm^3/g, respectively. The results also indicated that the isotherms belonged to type IV, revealing the presence of mesopores in ZnO. The obtained surface area of as-synthesized ZnO nanosponge was also larger than the previous reported ZnO nanostructures [14, 19, 20]. Above results demonstrated that the large surface area of ZnO nanosponge is anticipated for providing more effective photoactive surface sites for active radicals production and boosted the photocatalytic properties.

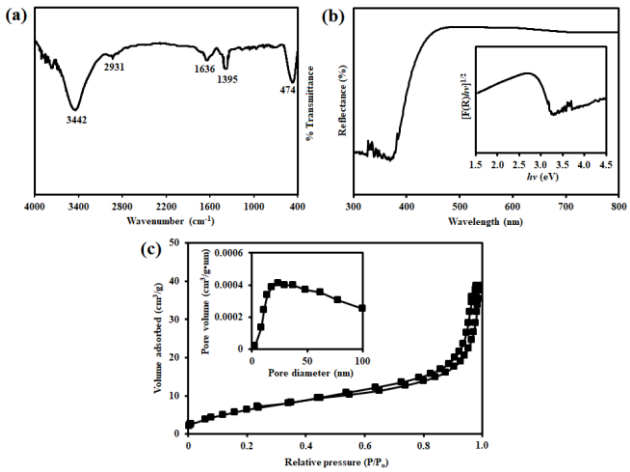

Fig. 3. (a) FTIR spectrum; (b) UV-vis DRS spectrum and (c) N2 adsorption–desorption isotherms and the corresponding pore size distribution (inset of c) of ZnO nanosponge. Inset of (b) is the plot of $(F(R)hv)^{1/2}$ vs. hv

3.2 Photodegradation of MB-RhB mixtures

The photoactivities of ZnO nanosponge were tested by MB-RhB mixtures degradation. MB and RhB are important organic dyes which largely utilized in textile, printing, pharmaceutical and food industries [21, 22]. Various studies have revealed that MB and RhB demonstrated toxicity, mutagenic, genotoxic and carcinogenic properties. Increased chromosomal

aberrations in *Muntiacus muntjac* and *Allium cepa* were also observed when exposed to these dyes [23, 24]. Therefore, MB and RhB were selected as model substrates in these photocatalytic activity tests. The optical absorption spectrum of MB-RhB mixtures over the ZnO nanosponge is shown in Fig. 4a. The RhB and MB showed strong absorption peak intensity (λ_{max}) at 554 nm and 666 nm, respectively. The λ_{max} of MB and RhB gradually decreased with increasing time intervals of light irradiation and disappeared after 180 min. Fig. 4b displays the efficiency of MB-RhB mixtures degradation as a function of irradiation duration. Only 2.9% RhB and 7.2% MB removal had been found in the absence of catalyst. This indicated that both dyes were stable under light irradiation. Under similar experimental conditions, a complete degradation of MB-RhB mixtures within 180 min was obtained over as-synthesized ZnO nanosponge. To investigate the effectiveness of the ZnO nanosponge, MB-RhB mixtures degradation over TiO_2-P25 was also carried out. It was clearly observed that only 85.6% of MB and 80.1% of RhB were degraded in the presence of TiO_2-P25 after 180 min irradiation. The reaction rate constants (k) of ZnO nanosponge and TiO_2-P25 for degradation of MB-RhB mixtures were determined based on first-order reaction kinetics $\ln(C_o/C) = kt$, where C_o is the equilibrium concentration of dye after 30 min dark adsorption and C is the concentration of dye after simulated solar light irradiation at equal time intervals t as shown in Fig. 4c. The results clearly indicated that the photodegradation rates of MB and RhB in the mixtures over the ZnO nanosponge were 0.0278 and 0.0174 min^{-1}, which were 2.5 and 1.9 times higher than that of TiO_2-P25 (0.0112 and 0.009 min^{-1} for MB and RhB, respectively). The high photodegradation performance of as-synthesized ZnO can be ascribed to the unique sponge-like porous morphology with large surface area that can provide large amount of photoactive surface sites and allowed the effective migration of charge carriers to the adsorbed species. These features were helpful to increase the quantity of •OH radicals for photoreaction and accelerated the MB-RhB mixtures degradation as indicated from the subsequent PL investigation in this work.

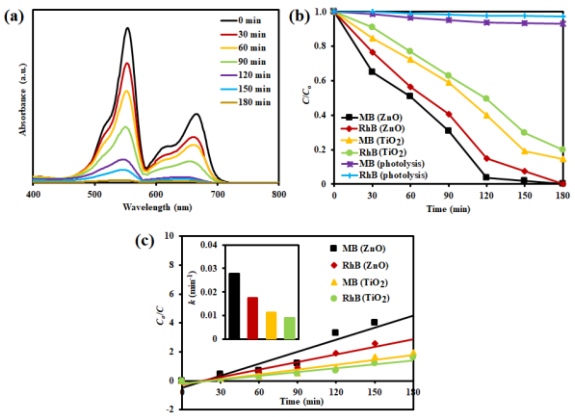

Fig. 4. (a) UV-vis absorption spectra of MB-RhB mixtures over ZnO nanosponge. (b) Relative concentration (C/C_o) vs. time plot of photodegradation of MB-RhB mixtures. (c) First-order kinetic plot of degradation of MB-RhB mixtures using different photocatalysts.

The COD concentration of the degraded solution was also evaluated to examine the performance of ZnO nanosponge on the mineralization of MB-RhB mixtures. As indicated in Fig. 5, the concentration of COD gradually reduced with increasing reaction time, indicating efficient decomposition of dye intermediates. After 180 min irradiation, the COD removal with ZnO nanosponge was 76.2%, whereas only 57.6% removal was achieved in the treatment with TiO_2-P25. Therefore, these results showed that ZnO nanosponge was more efficient as catalyst to induce the mineralization of MB-RhB mixtures.

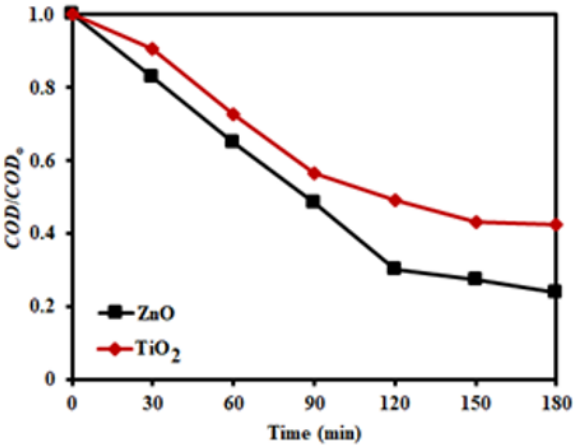

Fig. 5. COD removal during MB-RhB mixtures photodegradation.

3.3 Photodegradation of real textile dye wastewater

Fig. 6 depicts the photocatalytic performance of ZnO nanosponge in the degradation of textile dye wastewater. After 180 min irradiation, the photodegradation of textile dye wastewater decreased COD and BOD_5 concentrations by 66.9% and 60.1%, respectively. A low initial BOD_5/COD ratio of 0.16 also revealed the non-biodegradable characteristic of the wastewater and it was vital for considering the advanced oxidation processes. After photodegradation, an increase of BOD_5/COD ratio was observed and reached 0.20. Thus, this result evidenced the effectiveness of the developed photocatalytic system to enhance the biodegradability of treated textile dye wastewater as confirmed from the increase of the final BOD_5/COD ratio.

Table 1 also shows other quality parameters of textile dye wastewater after photocatalytically treated by ZnO nanosponge. It can be seen that the ammoniacal NH_3-N and colour removal efficiencies were 72.1% and 74.2%, respectively. Therefore, the ZnO nanosponge prepared using *Musa acuminata* peel extract benefited in the textile dye wastewater treatment.

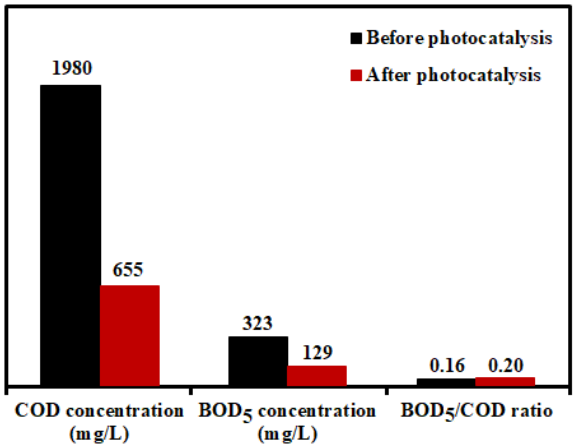

Fig. 6. COD concentration, BOD5 concentration as well as BOD_5/COD ratio of textile dye wastewater before and after ZnO nanosponge photocatalysis for 180 min.

Table 1. Quality parameters of textile dye wastewater before and after photocatalysis over ZnO nanosponge.

Parameter	As-received wastewater	After 180 min solar light	Removal efficiency (%)
COD (mg/L)	1980	655	66.9
BOD_5 (mg/L)	323	129	60.1
NH_3-N (mg/L)	4.3	1.2	72.1
Colour (Pt-Co)	837	216	74.2

3.4 Mechanism of photodegradation

With the obtained experimental results, a plausible schematic illustration was proposed to explain the photocatalytic activity of ZnO nanosponge (Fig. 7). When solar light was incident on the catalyst surface, the photogenerated electron-hole (e^--h^+) pairs were generated. The photogenerated conduction band e^- interacted with molecular oxygen stimulating the superoxide anion radicals (O_2•$^-$) formation and then transformed to •OH radicals. Similarly, the valence band h^+ scavenged by hydroxyl group to form •OH radicals. Due to •OH radicals being strong oxidizing agents, the dyes can be decomposed into simple species such as CO_2 and H_2O through continuous generated active radicals. The photocatalytic mechanism can be described as follows [25-27]:

$$ZnO + hv \rightarrow ZnO\ (e^- + h^+) \quad (1)$$

$$e^- + O_2 \rightarrow O_2^{\bullet-} \quad (2)$$

$$O_2^{\bullet-} + H^+ \rightarrow \bullet OOH \quad (3)$$

$$\bullet OOH + H^+ + e^- \rightarrow H_2O_2 \quad (4)$$

$$H_2O_2 + e^- \rightarrow \bullet OH + OH^- \quad (5)$$

$$h^+ + H_2O \rightarrow \bullet OH + H^+ \quad (6)$$

$$h^+ + OH^- \rightarrow \bullet OH \quad (7)$$

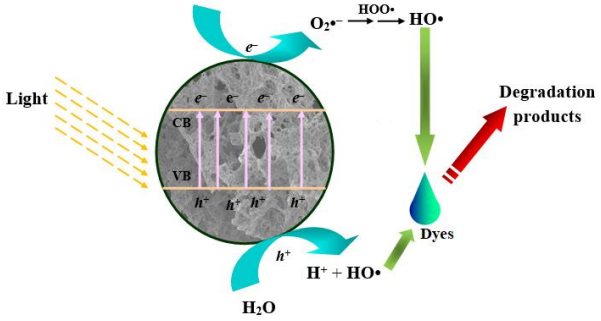

Fig. 7. Schematic illustration of photodegradation mechanism over the surface of ZnO nanosponge.

The abovementioned photocatalytic mechanism was further verified by the detection of •OH radicals with spectrofluorometer using TA as a standard probe molecule. Fig. 8a shows the PL emission spectra of different photocatalysts after 180 min irradiation. An obvious PL signal at 425 nm demonstrated the formation and involvement of •OH radicals in photodegradation. It was also obvious that the rate of •OH radicals formation over the ZnO nanosponge was higher than the TiO_2-P25, indicating the enhanced photocatalytic efficiency of the synthesized sample. Furthermore, Fig. 7b shows the variation in the PL intensity of ZnO nanosponge at different irradiation times. The unirradiated sample at 0 min revealed no PL emission, indicating that there was no formation of •OH radicals under dark conditions over the as-synthesized sample. However, the PL intensity increased linearly with irradiation time. This demonstrated that the •OH radicals were indeed generated on ZnO surface under solar light irradiation. Therefore, these results also evidenced that the highly active •OH radicals played significant role in dyes decomposition.

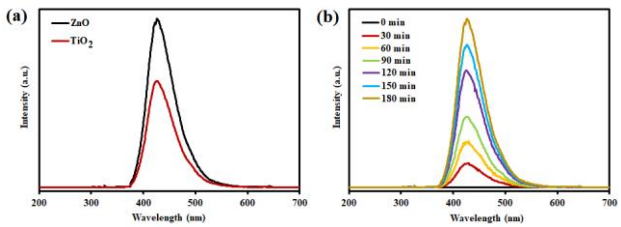

Fig. 8. (a) PL spectra of ZnO nanosponge and TiO_2-P25. (b) PL spectra changing with irradiation time over ZnO nanosponge.

4 Conclusion

In summary, we have first fabricated ZnO nanosponge by a *Musa acuminata* peel extract-mediated green synthetic route. The samples have been characterized by XRD, Raman, FESEM, EDX, FTIR, UV-vis DRS and N_2 adsorption-desorption measurements. Compared to TiO_2-P25, the as-synthesized ZnO nanosponge showed excellent MB-RhB mixtures degradation and mineralization which can be due to the enhancement of •OH radicals formation. In the case of real textile dye wastewater, the removal efficiencies of COD (66.9%), BOD_5 (60.1%), colour (74.2%) and NH_3-N (72.1%) were

achieved after 180 min of photocatalytic treatment. Hence, these results indicated that the biosynthesized ZnO nanosponge can act as efficient green photocatalyst in environmental remediation.

The authors would like to acknowledge the support from the Ministry of Higher Education, Malaysia (FRGS/1/2016/TK02/UTAR/02/1 and FRGS/1/2019/TK02/UTAR/02/4), Universiti Tunku Abdul Rahman (UTARRF/2019-C1/L03) and Guangxi Key Laboratory of Theory and Technology for Environmental Pollution Control (1801K012 and 1801K013) for this work

References

1. M.M. Ros, M.G. Dominguez, K.K.H. Aben, H.B.B. de-Mesquita, E. Kampman, S.H. Vermeulen, L.A. Kiemeney, Cancer Causes Control **23**, 1139 (2012).
2. V. Vaiano, M. Matarangolo, J.J. Murcia, H. Rojas, J.A. Navío, M.C. Hidalgo, Appl. Catal. B: Environ. **225**, 197 (2018).
3. T. Karnan, S.A.S. Selvakumar, J. Mol. Struct. **1125**, 358 (2016).
4. M. Eskandari, N. Goudarzi, S.G. Moussavi, Water Environ. J. **32**, 58 (2018).
5. X.Y. Bai, L.L. Li, H.Y. Liu, L.F. Tan, T.L. Liu, X.W. Meng, ACS Appl. Mater. Interfaces **7**, 1308 (2015).
6. M. Mittal, M. Sharma, O.P. Pandey, Sol. Energy **110**, 386 (2014).
7. M. Anbuvannan, M. Ramesh, G. Viruthagiri, N. Shanmugam, N. Kannadasan, Mater. Sci. Semicond. Process. **39**, 621 (2015).
8. S.S. Patil, M.G. Mali, M.S. Tamboli, D.R. Patil, M.V. Kulkarni, H. Yoon, H.Y. Kim, S.S. Al-Deyab, S.S. Yoon, S.S. Kolekar, B.B. Kale, Catal. Today **260**, 126 (2016).
9. S.A. Khan, F. Noreen, S. Kanwal, A. Iqbal, G. Hussain, Mater. Sci. Eng. C **82**, 46 (2018).
10. M.M. Wall, J. Food Compos. Anal. **19**, 434 (2006).
11. H.T. Vu, C.J. Scarlett, Q.V. Vuong, J. Funct. Foods **40**, 238 (2018).
12. P. Ilanchezhiyan, G.M. Kumar, M. Subramanian, R. Jayavel, Mater. Sci. Eng. B **175**, 238 (2010).
13. J. Zhao, L. Wang, X.Q. Yan, Y. Yang, Y. Lei, J. Zhou, Y.H. Huang, Y.S. Gu, Y. Zhang, Mater. Res. Bull. **46**, 1207 (2011).
14. F. Hosseini, A. Kasaeian, F. Pourfayaz, M. Sheikhpour, D.S. Wen, Mater. Sci. Semicond. Process. **83**, 175 (2018).
15. S.W. Liu, C. Li, J.G. Yu, Q.J. Xiang, CrystEngComm **13**, 2533 (2011).
16. S.K. Kansal, A.H. Ali, S. Kapoor, Desalination **259**, 147 (2010).
17. M. Stan, A. Popa, D. Toloman, A. Dehelean, I. Lung, G. Katona, Mater. Sci. Semicond. Process. **39**, 23 (2015).
18. S. Rajaboopathi, S. Thambidurai, Curr. Appl. Phys. **17**, 1622 (2017).
19. P. Amornpitoksuk, S. Suwanboon, S. Sangkanu, A. Sukhoom, N. Muensit, Superlattices Microstruct. **51**, 103 (2012).
20. S. Meephon, T. Rungrotmongkol, N. Kaiyawet, S. Puttamat, V. Pavarajarn, Catal. Lett. **148**, 873 (2018).
21. J.X. Guo, Z.Y. Wang, P. Sun, Q.Y. Tang, H.L. Li, X.Y. Wang, G.S. Guo, Q.S. Pu, Sens. Actuators B: Chem. **250**, 250 (2017).
22. N. Bordoloi, M.D. Dey, R. Mukhopadhyay, R. Kataki, Water Sci. Technol. **77**, 638 (2018).
23. I.L. Lewis, R.M. Patterson, H.C. McBay, Mutat. Res. **88**, 211 (1981).
24. P.A. Bedekar, S.D. Kshirsagar, A.R. Gholave, S.P. Govindwar, RSC Adv. **5**, 99228 (2015).
25. N.M. Ngoepe, Z. Mbita, M. Mathipa, M. Mketo, B. Ntsendwana, N.C. Hintsho-Mbita, Ceram. Int. **44**, 16999 (2018).
26. T.T. Bhosale, H.M. Shinde, N.L. Gavade, S.B. Babar, V.V. Gawade, S.R. Sabale, R.J. Kamble, B.S. Shirke, K.M. Garadkar, J. Mater. Sci.: Mater. Electron. **29**, 6826 (2018).
27. S.M. Lam, J.C. Sin, A.Z. Abdullah, A.R. Mohamed, Fuller. Nanotub. Car. N. **22**, 471 (2014).